Synergetic Effect between Photocatalysis on TiO$_2$ and Thermocatalysis on CeO$_2$ for Gas-Phase Oxidation of Benzene on TiO$_2$/CeO$_2$ Nanocomposites

Min Zeng, Yuanzhi Li,* Mingyang Mao, Jilin Bai, Lu Ren, and Xiujian Zhao

State Key Laboratory of Silicate Materials for Architectures, Wuhan University of Technology, 122 Luoshi Road, Wuhan 430070, P. R. China

Ⓢ Supporting Information

ABSTRACT: TiO$_2$/CeO$_2$ nanocomposites of anatase TiO$_2$ nanoparticles supported on microsized mesoporous CeO$_2$ were prepared and characterized by SEM, TEM, BET, XRD, Raman, XPS, and diffuse reflectance UV−vis absorption. The formation of the TiO$_2$/CeO$_2$ nanocomposites considerably enhances their catalytic activity for the gas-phase oxidation of benzene, one of the hazardous volatile organic compounds (VOCs), under the irradiation of a Xe lamp compared to pure CeO$_2$ and TiO$_2$. A solar-light-driven thermocatalysis on CeO$_2$ is found for the TiO$_2$/CeO$_2$ nanocomposites. There is a synergetic effect between the photocatalysis on TiO$_2$ and the thermocatalysis on CeO$_2$ for the TiO$_2$/CeO$_2$ nanocomposites, which significantly increases their catalytic activity. The CO$_2$ formation rate (r_{CO_2}) of the TiO$_2$/CeO$_2$ nanocomposite with the Ti/Ce molar ratio of 0.108 under the synergetic photothermocatalytic condition is 36.4 times higher than its r_{CO_2} under the conventional photocatalytic condition at near room temperature. CO temperature-programmed reduction (CO-TPR) with the irradiation of the Xe lamp and in the dark reveals that the synergetic effect, which occurs at the interface of the TiO$_2$/CeO$_2$ nanocomposite, is due to the considerable promotion of the CeO$_2$ reduction by the photocatalysis on TiO$_2$.

KEYWORDS: TiO$_2$, TiO$_2$/CeO$_2$ nanocomposite, photocatalysis, thermocatalysis, photothermocatalysis, synergetic effect, VOCs
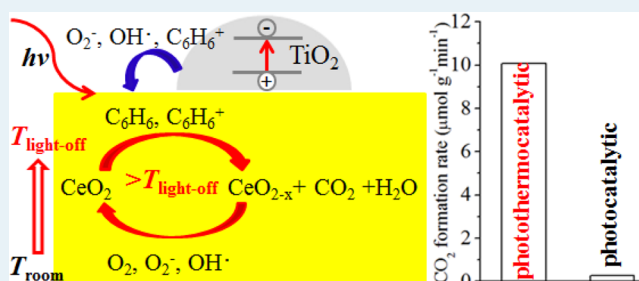
1. INTRODUCTION

Volatile organic compounds (VOCs) are major air pollutants in indoor air, polluted urban atmospheres, factories of petrochemical, fine chemical, paint, and so on, and are harmful to human health as well as to the environment. It is highly desirable to develop efficient technology for the abatement of VOCs.[1,2] Heterogeneous photocatalysis by nano semiconductors is a promising technology for the abatement of VOCs because it is energy-saving, and operates under mild conditions—at ambient temperature, atmospheric pressure, and using oxygen (air) as the oxidizing agent. Among the various photocatalysts, nanostructured TiO$_2$ is one of the most prominent photocatalysts due to its excellent catalytic performance, chemical stability, low cost, and nontoxicity.[3] However, there are three bottlenecks which greatly retard its extensive application for the removal of VOCs. One is its low quantum efficiency due to fast recombination of photogenerated electrons and holes.[4,5] The other is that it is only photoactivated by UV, which accounts for ∼5% of the sunlight, due to its wide band gap (3.2 eV for anatase, and 3.0 eV for rutile).[6−8] The two disadvantages make the photocatalysis only efficient for the removal of low concentration VOCs. The third is that it is prone to deactivation mainly due to the deposition of less reactive byproducts on the TiO$_2$ surface.[9−11] Another efficient

technology for the removal of VOCs is heterogeneous thermocatalysis, which has been widely applied in industry. Expensive noble metals are conventionally used as the most efficient thermocatalysts.[12] The main advantages of thermocatalysis are that it is efficient for the removal of high concentration VOCs and has good thermocatalytic durability. However, compared to photocatalysis, thermocatalysis is energy-consuming and must operate at higher temperature by using an additional heater. Therefore, finding a novel strategy for the efficient abatement of VOCs with the advantages of both photocatalysis and thermocatalysis, which could utilize renewable solar energy and avoid their disadvantages, would be scientifically and technologically significant.

Nanostructured CeO$_2$ is one of the efficient thermocatalysts, in addition to the expensive noble metals, for the removal of air pollutants including VOCs, owing to its remarkable Ce^{4+}/Ce^{3+} redox properties.[13−20] Its thermocatalytic activity can be improved by controlling the size, exposed facets (e.g., {100}, {110}),[14−16] and surface structure, such as oxygen vacancies,[17−20] among others. On the other hand, nanostructured

Scheme 1. Schematic Diagram of the Photothermocatalytic Setup
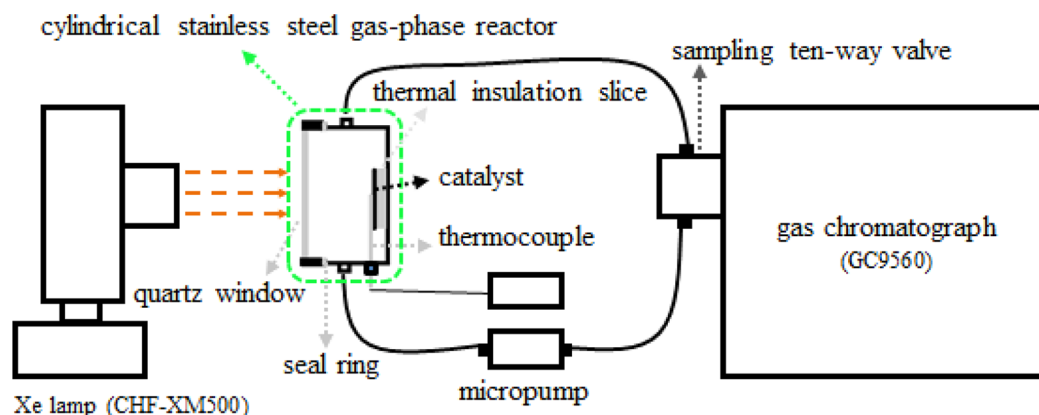
CeO$_2$ as n-type semiconductor with band gap narrower than TiO$_2$ has photocatalytic activity under UV and/or visible irradiation,[21−24] and its photocatalytic activity can be improved by controlling its morphology, doping metal ions,[25,26] and forming a nanocomposite with TiO$_2$ to increase e-h separation efficiency.[27−39] Recently, a synergetic effect of photo/thermocatalysis was reported by several groups. With the synergetic effect, significant enhancement in the catalytic activity was achieved on mesoporous CeO$_2$[40] and Mn-, Bi-doped CeO$_2$[41,42] for the abatement of VOCs such as benzene, formaldehyde, and on Y-doped CeO$_2$ for the photodegradation of dye.[43]

Recently, we developed a facile template-free approach to synthesize microsized mesoporous CeO$_2$, and we reported that the microsized mesoporous CeO$_2$ exhibited a significant enhancement of thermocatalytic activity as compared to CeO$_2$ nanoparticles and nanocubes without mesopores.[20] Herein, we load TiO$_2$ nanoparticles on the microsized mesoporous CeO$_2$ to form TiO$_2$/CeO$_2$ nanocomposites. We achieve a perfect combination of photocatalysis and thermocatalysis on the TiO$_2$/CeO$_2$ nanocomposites. They exhibit efficient catalytic activity for the gas-phase benzene oxidation under the full solar spectrum irradiation and visible-infrared irradiation. A solar-light-driven thermocatalysis on CeO$_2$ is found for the TiO$_2$/CeO$_2$ nanocomposites. We find a novel synergetic effect between the light-driven thermocatalysis on CeO$_2$ and the photocatalysis on TiO$_2$ for the TiO$_2$/CeO$_2$ nanocomposites, which considerably increases their catalytic activity. We reveal that the synergetic effect, occurring at the interface of the TiO$_2$/CeO$_2$ nanocomposites, is due to the considerable promotion of the CeO$_2$ reduction by the photocatalysis on TiO$_2$.

2. EXPERIMENTAL SECTION

Preparation. Microsized mesoporous CeO$_2$ was prepared according to the procedure reported in our previous work:[20] Sixty g of Ce(NO$_3$)$_3$·6H$_2$O and 24.896 g of urea were added into 160 mL of distilled water under magnetic stirring until they were dissolved. Then, the solution was added to a 200 mL Teflon bottle, which was sealed tightly in a stainless-steel autoclave. The autoclave was put in an electric oven, heated to 180 °C, and kept at 180 °C for 16 h. After the autoclave cooled to ambient temperature, the precipitate was thoroughly washed with distilled water and dried at 90 °C for 12 h. The obtained powder was the uncalcined ceria. Finally, the powder was calcined at 400 °C for 4 h in a Muffle furnace.

TiO$_2$/CeO$_2$ samples with different Ti/Ce molar ratio were prepared according to the following procedure: A known amount of titanium butoxide (e.g., 0, 0.341, 0.852, 1.705 g) was dissolved to 70 mL of ethanol in a beaker. Uncalcined ceria (4.742 g) was added to the titanium butoxide solution. The beaker was placed into a water bath at 70 °C. The mixture was magnetically stirred until the ethanol was evaporated. The product was thoroughly washed with distilled water, dried at 90 °C for 12 h in an electric oven, and finally calcined at 400 °C for 4 h in a Muffle furnace. The obtained TiO$_2$/CeO$_2$ samples with Ti/Ce molar ratio of 0.043, 0.108, 0.216 in reactants are denoted as TiO$_2$/CeO$_2$-A, TiO$_2$/CeO$_2$-B, TiO$_2$/CeO$_2$-C, respectively.

Pure nano TiO$_2$ was prepared by the same procedure as the TiO$_2$/CeO$_2$ samples, except without addition of the uncalcined ceria.

Characterization. SEM images and energy dispersive X-ray spectroscopy (EDX) were obtained with a ULTRA PLUS-43-13 scanning electron microscope. Transmission electron microscopy (TEM) images were obtained on a JEM-100CX electron microscope. The measurement of surface area was conducted by using N$_2$ adsorption at −196 °C on ASAP2020. X-ray diffraction (XRD) was taken on a Rigaku Dmax X-ray diffractometer with Cu Kα radiation. Raman spectra were recorded on a Renishaw inVia Raman microscope with the excitation of 514.5 nm laser light. X-ray photoelectron spectroscopy (XPS) analysis was taken on a VG Multilab 2000 X-ray photoelectron spectrometer with Mg Kα radiation. Diffuse reflectance UV−vis absorption was measured on a UV-3600 spectrophotometer.

CO temperature-programmed reduction (CO-TPR) was performed on a TP-5080 multifunctional adsorption apparatus equipped with a TCD detector. The sample was put in a tubular quartz reactor. A quartz window was connected to one of the end of the quartz reactor. A Xe lamp (CHF-XM500) was put in the front of the quartz window. The samples were pretreated in 5 vol % O$_2$/He at 200 °C for 1 h. CO-TPR was conducted by heating the pretreated samples in the flow of 5 vol % CO/He with the irradiation of the Xe lamp or in dark.

Photothermocatalytic Activity. The photothermocatalytic activity of the samples for benzene oxidation was measured on a closed cylindrical stainless-steel gas-phase reactor with a quartz window under the irradiation of a Xe lamp (CHF-XM500) as schematically illustrated in Scheme 1. To reduce energy loss during the irradiation, 0.1000 g of the sample was coated on a thermal insulation slice. To measure the

photothermocatalytic activity under the visible-infrared irradiation from the Xe lamp, a cutoff filter that can filter out the irradiation with wavelength less than 420 or 480 nm was placed between the Xe lamp and the quartz window. The products and reactants were analyzed by gas chromatograph. The experimental procedure and the light intensity from the Xe lamp were detailed in our recently published work.[44]

Photocatalytic Activity. The photocatalytic activity of the samples for the oxidation of benzene under the Xe lamp irradiation at near ambient temperature was measured according to the procedure described in our recent publications.[44]

Thermocatalytic Activity. The thermocatalytic activity of the samples for the oxidation of benzene was tested in a continuous-flow fixed-bed quartz tubular reactor at different temperatures. The experimental procedure was detailed in our previous publication.[2]

3. RESULTS AND DISCUSSION

3.1. Characterization. The TiO_2/CeO_2 nanocomposites with different Ti/Ce molar ratio were prepared by loading different amount of TiO_2 nanoparticles on the microsized mesoporous CeO_2. Figure 1 shows SEM images with the
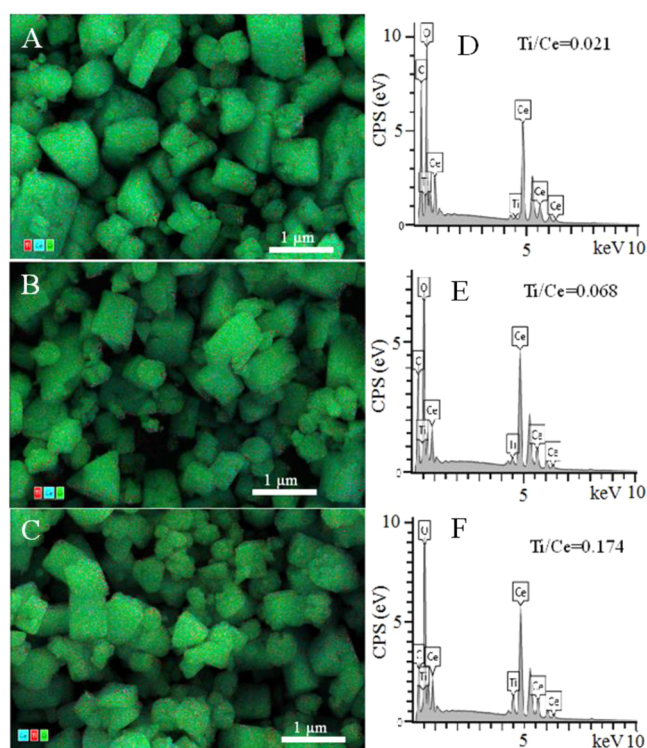
Figure 1. SEM images with the distribution of elements and EDX of TiO_2/CeO_2 —A (A, D), TiO_2/CeO_2-B (B, E), and TiO_2/CeO_2-C (C, F): Ti (red), Ce (cyan), and O (green).

distribution of elements and energy-dispersive X-ray spectroscopy of the TiO_2/CeO_2 samples. As shown in Figure 1, titanium is well distributed on the microsized CeO_2 for all the TiO_2/CeO_2 samples (Figure 1A−C). This is confirmed by the SEM images with the separate distribution of Ti, Ce, and O for the TiO_2/CeO_2 samples (Figure S1, Supporting Information). Ce, O, Ti, and adventitious carbon are detected by EDX (Figure 1D−F). The Ti/Ce molar ratio of TiO_2/CeO_2-A, TiO_2/CeO_2-B, and TiO_2/CeO_2-C is 0.021, 0.068, 0.174,

respectively (Table 1), which is slightly lower than the corresponding data in reactants (0.043, 0.108, 0.216). This is due to the diffusion of titanium butoxide into the pores of the microsized mesoporous CeO_2 during the preparation (see Experimental Section). Figure 2 shows TEM images of the
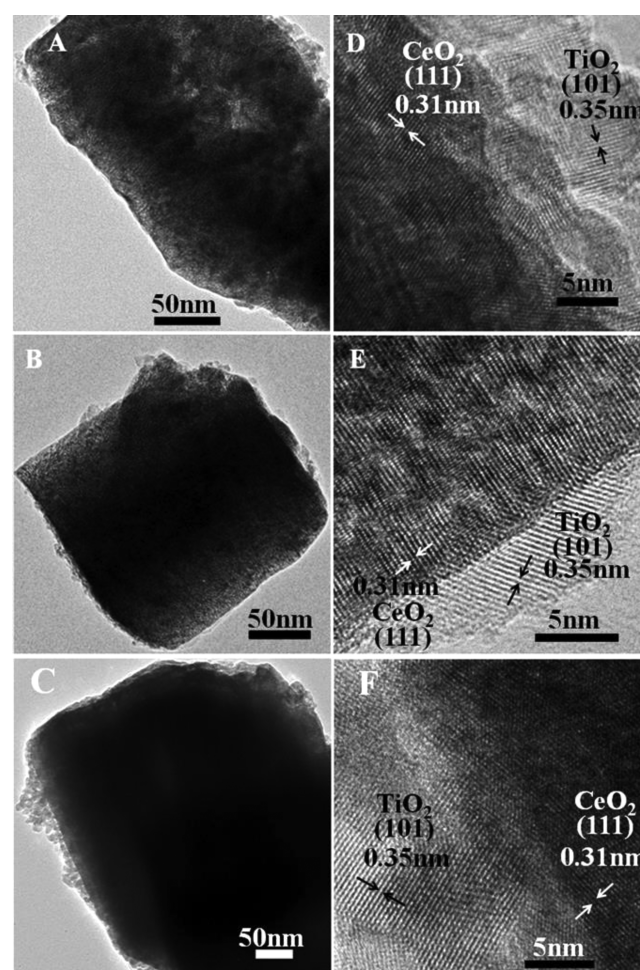
Figure 2. TEM images of TiO_2/CeO_2 −A (A, D), TiO_2/CeO_2-B (B, E), and TiO_2/CeO_2-C (C, F).

TiO_2/CeO_2 samples. TiO_2 nanoparticles are observed on microsized mesoporous CeO_2. With an increase in the Ti/Ce molar ratio from 0.043 to 0.108, 0.216, more TiO_2 nanoparticles are observed. When the Ti/Ce molar ratio increases to 0.216 (TiO_2/CeO_2-C, Figure 2C), a thin layer of TiO_2 nanoparticles formed on microsized CeO_2 was observed . The size of TiO_2 nanoparticles in the TiO_2/CeO_2 samples is estimated by TEM to be 2−17 nm. In this case, mesopores cannot be observed on microsized CeO_2 as they are blocked by TiO_2 nanoparticles. HRTEM shows that TiO_2 nanoparticles with {101} planes of anatase for all the TiO_2/CeO_2 samples are closely contacted to CeO_2 with {111} planes. This result indicates the formation of TiO_2/CeO_2 nanocomposites of anatase TiO_2 nanoparticles supported on microsized mesoporous CeO_2.

The N_2 adsorption−desorption isotherm indicates that the TiO_2/CeO_2 samples have a desorption hysteresis due to the capillary condensation of N_2 in pores (Figure S2). The dominant pore size of CeO_2, TiO_2/CeO_2-A, TiO_2/CeO_2-B, TiO_2/CeO_2-C is 3.8, 1.5, 1.5, 1.3 nm, respectively (Figure S2,

Table 1. Ti/Ce Molar Ratio, BET Surface Area, Pore Volume, Dominant Pore Size, and Ce^{3+} Fraction of the Samples

sample	Ti/Ce molar ratio in reactants by	EDX	BET surface area (m^{2}g^{-1})	pore volume (cm^{3}g^{-1})	dominant pore size (nm)	Ce^{3+}/(Ce^{3+}+Ce^{4+}) molar ratio by XPS
CeO$_2$			84.0	0.055	3.8	0.30
TiO$_2$/CeO$_2$-A	0.043	0.021	71.6	0.059	1.5	0.31
TiO$_2$/CeO$_2$-B	0.108	0.068	70.3	0.057	1.5	0.33
TiO$_2$/CeO$_2$-C	0.216	0.174	73.1	0.061	1.3	0.35

Table 1). Their corresponding total pore volume is 0.0545, 0.0589, 0.0575, 0.0612 cm^3 g^{-1}, respectively. The BET surface area of CeO$_2$, TiO$_2$/CeO$_2$-A, TiO$_2$/CeO$_2$-B, TiO$_2$/CeO$_2$-C is 84.0, 71.6, 70.3, 73.1 m^2 g^{-1}, respectively (Table 1).

The XRD analysis reveals that CeO$_2$ in all the TiO$_2$/CeO$_2$ samples has a cubic fluorite structure (JCPDS 89-8436), as shown in Figure 3A. There is a weak peak observed at 25.3° for
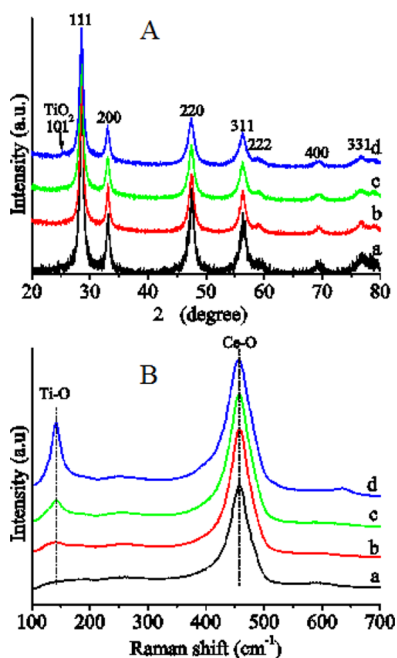
Figure 3. XRD pattern (A) and Raman spectra (B) of CeO$_2$ (a), TiO$_2$/CeO$_2$-A (b), TiO$_2$/CeO$_2$-B (c), and TiO$_2$/CeO$_2$-C (d).

TiO$_2$/CeO$_2$-C with higher Ti/Ce molar ratio of 0.216 (Table 1), which belongs to {101} planes of anatase (JCPDS 89−4921). This is in agreement to the observation by HRTEM. But no XRD peaks of anatase are observed for TiO$_2$/CeO$_2$-A and TiO$_2$/CeO$_2$-B with lower Ti/Ce molar ratio (Table 1). This is attributed to the lower fraction of anatase in the TiO$_2$/CeO$_2$ nanocomposites than the detection limit by XRD. Figure 3B shows the Raman spectra of the samples. For TiO$_2$/CeO$_2$-A, there is a weak Raman peak observed around ∼143 cm^{-1}, which is attributed to the Eg mode of anatase.[11,45] Increasing the Ti/Ce molar ratio from 0.043 to 0.108 and 0.216 leads to a gradual enhancement of the intensity for the Eg mode of anatase.

Figure 4A shows diffuse reflectance UV−vis spectra of the samples. The microsized mesoporous CeO$_2$ and TiO$_2$/CeO$_2$ nanocomposites have absorption up to ∼500 nm. The visible absorption is attributed to the presence of Ce^{3+} in the microsized mesoporous CeO$_2$ and TiO$_2$/CeO$_2$ samples[40,46] as the band gap of CeO$_2$, which is due to the indirect O2p−Ce4f transition along the L high-symmetry lines of the Brillouin
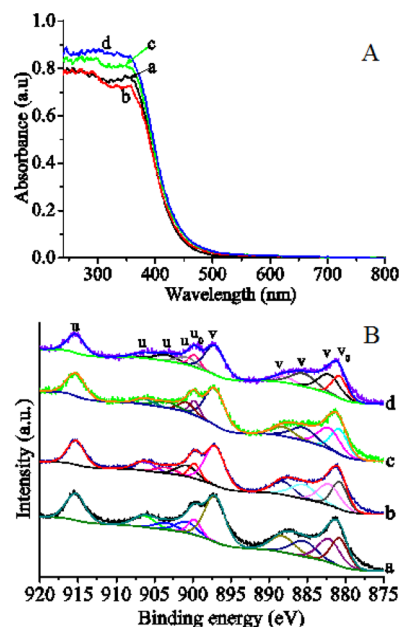
Figure 4. Diffuse reflectance UV−vis absorption (A) and Ce 3d XPS spectra (B) of CeO$_2$ (a), TiO$_2$/CeO$_2$-A (b), TiO$_2$/CeO$_2$-B (c), and TiO$_2$/CeO$_2$-C (d).

zone, is correlated with the Ce^{3+} concentration.[46] The existence of Ce^{3+} in the samples is confirmed by analyzing their Ce 3d XPS spectra (Figure 4B). Six peaks labeled as v, v″, v‴ (3d$_{5/2}$), u, u″, u‴ (3d$_{3/2}$) referring to three pairs of spin−orbit doublets are characteristic of Ce^{4+}3d. Four peaks labeled as v$_0$, v′(3d$_{5/2}$), u$_0$, u′ (3d$_{3/2}$) correspond to Ce^{3+}3d.[27,47] The molar ratio of Ce^{3+}/(Ce^{3+}+Ce^{4+}) in CeO$_2$, TiO$_2$/CeO$_2$-A, TiO$_2$/CeO$_2$-B, and TiO$_2$/CeO$_2$-C is estimated by the deconvolution of their Ce 3d XPS spectra to be 0.30, 0.31, 0.33, 0.35 (Table 1), respectively.

3.2. Photothermocatalytic Activity. The photocatalytic activity of the samples was measured by evaluating the rate of CO$_2$ formation from the gas-phase oxidation of benzene under the irradiation of a Xe lamp. The catalytic oxidation of benzene is chosen as benzene is carcinogenic and recalcitrant, and one of the main VOC pollutants. As shown in Figure 5A, the microsized mesoporous CeO$_2$ exhibits efficient catalytic activity for benzene oxidation. After the irradiation for 60 min, the concentration of CO$_2$ produced is 3587.4 mg m^{-3}. Loading a small amount of TiO$_2$ nanoparticles on the microsized mesoporous CeO$_2$ (TiO$_2$/CeO$_2$-A) leads to a significant enhancement of its photocatalytic activity. After the irradiation for 60 min, the concentration of CO$_2$ produced increases from 3587.4 to 5303.8 mg m^{-3}. Increasing the Ti/Ce molar ratio from 0.043 to 0.108 results in a further improvement in the photocatalytic activity. After the irradiation for 60 min, the concentration of CO$_2$ produced increases to 5954.8 mg m^{-3} (TiO$_2$/CeO$_2$-B). However, further enhancing the Ti/Ce molar ratio to 0.216 does not increase the photocatalytic activity.
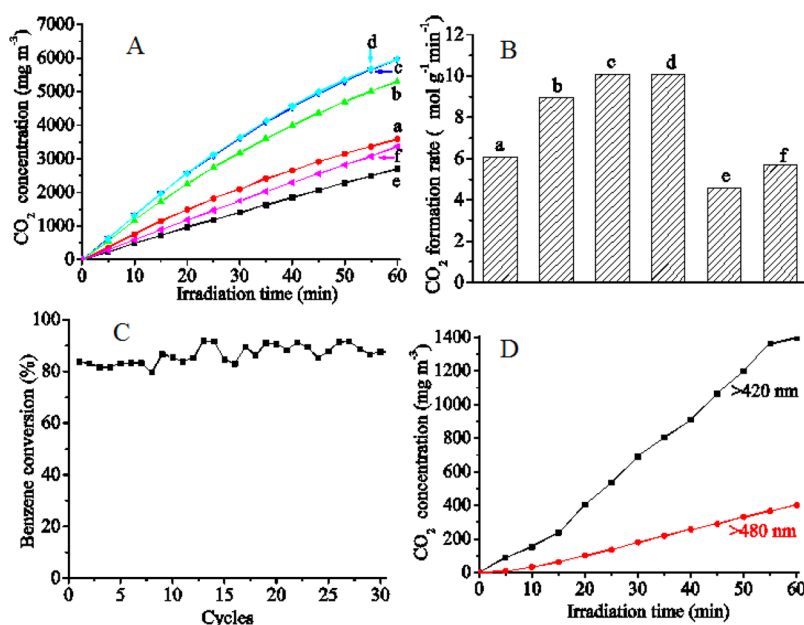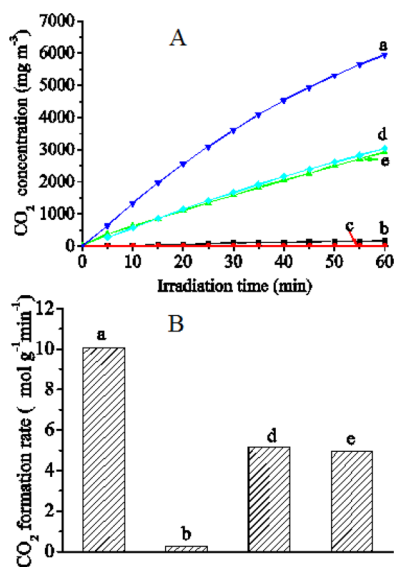
Figure 5. Time course of CO_2 produced from benzene oxidation (A), r_{CO_2} for benzene oxidation on the catalysts (B), the durability of TiO_2/CeO_2-B for the benzene oxidation (the reaction time of every cycle, 60 min) under the Xe lamp irradiation (C), and time course of CO_2 produced from benzene oxidation on TiO_2/CeO_2-B under the irradiation above 420 or 480 nm (D): CeO_2(a), TiO_2/CeO_2-A (b),TiO_2/CeO_2-B (c), TiO_2/CeO_2-C (d), TiO_2(P25) (e), and TiO_2(f).

TiO_2/CeO_2-C has the almost same photocatalytic activity as TiO_2/CeO_2-B. This means that the optimum Ti/Ce molar ratio is 0.108 for the TiO_2/CeO_2 nanocomposites. It is well-known that TiO_2 (P25), a mixture of anatase (80%) with band gap of 3.2 eV and rutile (20%) with band gap of 3.0 eV,[3] exhibits very good photocatalytic activity under UV irradiation; thus, it is widely used as benchmark photocatalyst. For comparison, we measured the photocatalytic activity of TiO_2(P25) for benzene oxidation under the irradiation of the Xe lamp. After the irradiation for 60 min, the concentration of CO_2 produced is 2706.4 mg m^{-3}. Its photocatalytic activity is much lower than the microsized mesoporous CeO_2 and the TiO_2/CeO_2 nanocomposites. We also measured the photocatalytic activity of pure nano TiO_2 for benzene oxidation under the irradiation of the Xe lamp. The pure nano TiO_2 has anatase crystalline structure with band gap of 3.2 eV and its BET surface area is 46.9 m^2 g^{-1}. After the irradiation for 60 min, the concentration of CO_2 produced is 3362.9 mg m^{-3}. Its photocatalytic activity is much lower than the TiO_2/CeO_2 nanocomposites. Figure 5B shows the CO_2 formation rate per unit mass of catalyst (r_{CO_2}). r_{CO_2} of TiO_2/CeO_2-B (10.1 μmol g^{-1} min^{-1}) is 1.7, 2.2, 1.8 times higher than CeO_2, TiO_2(P25), nano TiO_2, respectively. As the catalyst has different surface area (Table 1), we calculate the rate of CO_2 formation rate per unit surface area of catalyst (r_{SCO_2}). r_{SCO_2} of TiO_2/CeO_2-B (0.14 μmol m^{-2} min^{-1}) is 2.0, 1.8 times higher than CeO_2 and TiO_2(P25), respectively. This result reveals that the formation of the TiO_2/CeO_2 nanocomposites considerably enhances its photocatalytic activity. The photocatalytic durability of TiO_2/CeO_2-B for benzene oxidation under the irradiation of the Xe lamp was tested. As shown in Figure 5C, its photocatalytic activity keeps unchanged when the catalyst was recycled for 30 times, suggesting that TiO_2/CeO_2-B exhibits a good photocatalytic durability.

As the TiO_2/CeO_2 nanocomposites have absorption up to ~500 nm (Figure 4), in order to confirm whether they exhibit

visible photocatalytic activity, we measured the photocatalytic activity of TiO_2/CeO_2-B for benzene oxidation under the visible-infrared irradiation above 420 or 480 nm from the Xe lamp. As shown in Figure 5D, TiO_2/CeO_2-B exhibits photocatalytic activity under the visible-infrared irradiation above 420 or 480 nm. After the visible-infrared irradiation above 420 or 480 nm for 60 min, the concentration of CO_2 produced is 1398.3, 401.1 mg m^{-3}, respectively. The r_{CO_2} of TiO_2/CeO_2-B under the visible-infrared irradiation above 420 or 480 nm is 2.37, 0.68 μmol g^{-1} min^{-1}, respectively. The considerable decrease of the photocatalytic activity is attributed to the decreased absorption above 420 or 480 nm for $TiO_2/$ CeO_2-B (Figure 4A).
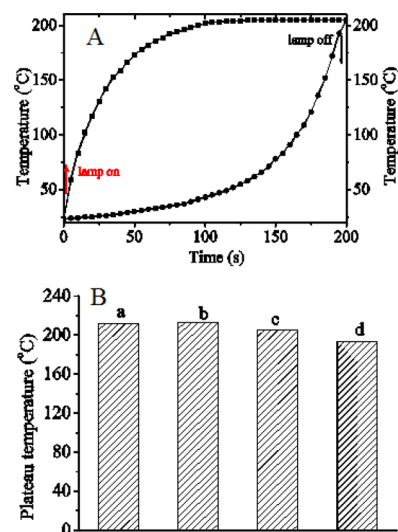
3.3. Mechanism. Nano TiO_2 has been regarded as one of the most effective UV photocatalysts.[3] Some researchers reported that nano CeO_2 shows photocatalytic activity under UV or visible irradiation.[21−24] The photodegradation of organic pollutants on TiO_2 follows the well-known photocatalytic mechanism.[3] To confirm whether the TiO_2/CeO_2 nanocomposites follow the conventional photocatalytic mechanism, the photocatalytic activity of CeO_2 and TiO_2/CeO_2-B for benzene oxidation under the Xe lamp irradiation at near ambient temperature was measured. As can be seen from Figure 6, TiO_2/CeO_2-B shows photocatalytic activity, whereas CeO_2 has almost no photocatalytic activity for benzene oxidation at ~40 °C. But, the r_{CO_2} of TiO_2/CeO_2-B under photothermocatalytic condition is 36.4 times higher than that of TiO_2/CeO_2-B under the photocatalytic condition at ~40 °C (Figure 6). This result clearly indicates the presence of a solar-light-driven thermocatalysis (schematically illustrated in Scheme 2) except for the photocatalysis for benzene oxidation on TiO_2/CeO_2-B under the irradiation of the Xe lamp: The irradiation of the Xe lamp on the TiO_2/CeO_2 nanocomposites results in a considerable increase of their temperature due to the photothermal conversion and the infrared heating effect

Figure 6. Time course of CO_2 produced from benzene oxidation (A) and r_{CO_2} for benzene oxidation on the catalysts (B) under the different cases: TiO_2/CeO_2-B under the Xe lamp irradiation (*photothermocatalytic*, a), TiO_2/CeO_2-B (b) and CeO_2 (c) under the Xe lamp irradiation at near room temperature (*photocatalytic*), TiO_2/CeO_2-B under the irradiation above 420 nm with higher light intensity (d), a mixture of TiO_2 and CeO_2 with the same Ti/Ce molar ratio as TiO_2/CeO_2-B under the Xe lamp irradiation (e).

Figure 7. Temporal evolution of the temperature on TiO_2/CeO_2-B (A) and the plateau temperature of the samples (B) under the Xe lamp irradiation: CeO_2 (a), TiO_2/CeO_2-A (b), TiO_2/CeO_2-B (c), and TiO_2/CeO_2-C (d).

(See 3.3.1 **Photothermal conversion**). When the temperature increases to the thermocatalytic light-off temperature ($T_{light-off}$) of the TiO_2/CeO_2 nanocomposites, the thermocatalytic oxidation of benzene starts (see 3.3.2 **Thermocatalysis**).

3.3.1. Photothermal Conversion. To prove the solar-light-driven thermocatalysis, first, we measured the temperature evolution of the samples with the irradiation of the Xe lamp. Under the Xe lamp irradiation, the temperature of all the samples quickly increases to a plateau (Figure 7A). The temperature increase is attributed to the photothermal conversion due to the absorption of the UV−visible irradiation

by the samples (Figure 4A) as well as the heating effect of the infrared irradiation from the Xe lamp. When the photothermal conversion and the heating effect establish equilibrium with the energy dissipation from the sample to the surroundings, a plateau temperature is observed. The plateau temperature of CeO_2, TiO_2/CeO_2-A, TiO_2/CeO_2-B, TiO_2/CeO_2-C is 212, 213, 205, 193 °C, respectively (Figure 7B). This result indicates a slight decrease of the plateau temperature with increasing the Ti/Ce molar ratio, which is due to the reflectance of the infrared light by TiO_2 as white pigment. The temperature evolution of TiO_2/CeO_2-B under the irradiation above 420 and 480 nm was also measured. In this case, the plateau temperature under the irradiation above 420 and 480 nm is 188, 174 °C, respectively.

3.3.2. Thermocatalysis. To confirm whether the plateau temperature of the catalysts can reach to the light-off

Scheme 2. Schematic Illustration of Solar-Light-Driven Thermocatalysis and the Synergetic Effect between the Photocatalysis on TiO_2 and Thermocatalysis on CeO_2 for the TiO_2/CeO_2 Nanocomposites
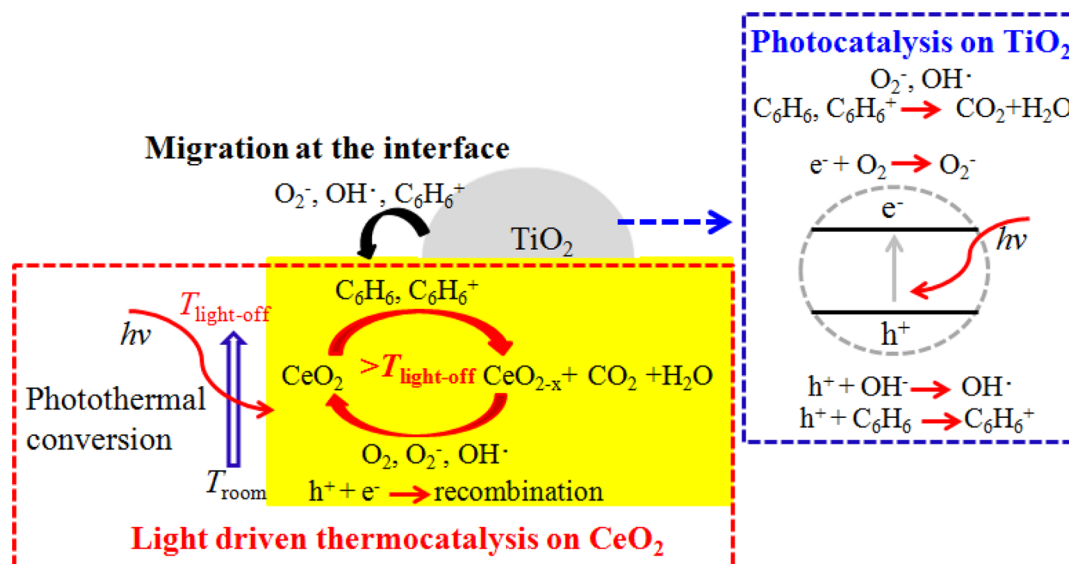
temperature ($T_{\text{light-off}}$) for benzene oxidation, we studied the effect of reaction temperature on the thermocatalytic activity of the catalysts for the oxidation of benzene in a flow fixed-bed reactor. As shown in Figure 8, compared to the thermocatalytic
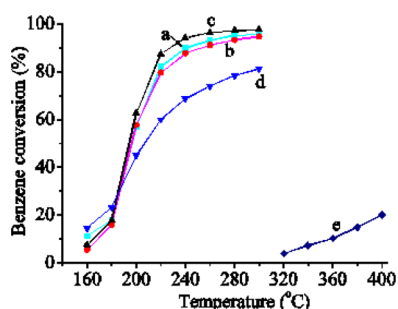
Figure 8. Benzene conversion versus reaction temperature over the catalysts for benzene oxidation under the condition of benzene concentration = 2.0 g m^{-3}, space velocity (SV) = 48 000 mL g^{-1} $_{\text{catalyst}}$ h^{-1}, ambient pressure: CeO$_2$ (a), TiO$_2$/CeO$_2$-A (b), TiO$_2$/CeO$_2$-B (c), TiO$_2$/CeO$_2$-C (d), and nano TiO$_2$ (e).

activity of the microsized mesoporous CeO$_2$, loading a small amount of TiO$_2$ nanoparticles on the microsized mesoporous CeO$_2$ (TiO$_2$/CeO$_2$-A, TiO$_2$/CeO$_2$-B) does not obviously alter its thermocatalytic activity. Further increasing the Ti/Ce molar to 0.216 (TiO$_2$/CeO$_2$-C) leads to a decrease of thermocatalytic activity above ~200 °C due to the much lower thermocatalytic activity of the nano TiO$_2$ (Figure 8, curve e) than CeO$_2$. For the microsized mesoporous CeO$_2$ and all the TiO$_2$/CeO$_2$ nanocomposites, benzene starts to be oxidized around ~160 °C. All the plateau temperatures of the microsized mesoporous CeO$_2$ and the TiO$_2$/CeO$_2$ nanocomposites under the Xe lamp irradiation (Figure 7B) are higher than their corresponding $T_{\text{light-off}}$ (~160 °C). Thus, the solar-light-driven thermocatalytic oxidation of benzene can take place. The plateau temperature of TiO$_2$/CeO$_2$-B under the irradiation above 420 or 480 nm is higher than its corresponding $T_{\text{light-off}}$. This is why TiO$_2$/CeO$_2$-B exhibits visible-infrared light-driven thermocatalytic activity for benzene oxidation.

3.4. Synergetic Effect. We tested the photocatalytic activity of TiO$_2$/CeO$_2$-B under the irradiation above 420 nm with higher irradiation intensity by reducing the distance between the Xe lamp and the reactor (Figure 6). By increasing the visible-infrared irradiation intensity, its plateau temperature is equal to that under the full solar spectrum irradiation of the Xe lamp (205 °C, Figure 7). In this case, only visible-infrared light-driven thermocatalysis on CeO$_2$ occurs as anatase TiO$_2$ cannot be photoactivated by the visible irradiation above 420 nm because of its large band gap (3.2 eV, 386 nm). Its thermocatalytic activity should be the same as under the full solar spectrum irradiation of the Xe lamp. Interestingly, r_{CO_2} of TiO$_2$/CeO$_2$-B under the full solar spectrum irradiation is 1.9 times higher than the sum of its r_{CO_2} under the irradiation above 420 nm with higher irradiation intensity (5.15 μmol g^{-1} min^{-1}) and its r_{CO_2} under the full solar spectrum irradiation at near ambient temperature. This result suggests the presence of a synergetic effect between the light-driven thermocatalysis on CeO$_2$ and the photocatalysis on TiO$_2$ for TiO$_2$/CeO$_2$-B under the full solar spectrum irradiation

In order to further prove the synergetic effect, we tested the photocatalytic activity of a mixture of the nano TiO$_2$ and the

microsized mesoporous CeO$_2$ with the same Ti/Ce molar ratio as TiO$_2$/CeO$_2$-B under the Xe lamp irradiation. In this case, r_{CO_2} of the mixture of the nano TiO$_2$ and the microsized mesoporous CeO$_2$ (4.95 μmol g^{-1} min^{-1}) is 2.0 times lower than that of TiO$_2$/CeO$_2$-B (Figure 6). These results undoubtedly indicate that there is a synergetic effect between the light-driven thermocatalysis on CeO$_2$ and the photocatalysis on TiO$_2$ for TiO$_2$/CeO$_2$-B, and the synergetic effect takes place at the interface of the TiO$_2$/CeO$_2$ nanocomposites, as schematically illustrated in Scheme 2.

Upon UV excitation, electrons on the valence band of TiO$_2$ are excited to the conduction band, leaving a hole on the valence band. The photogenerated holes and electrons move to the surface of TiO$_2$. The electrons reduce the electron acceptor (e.g., O$_2$) adsorbed on the surface of TiO$_2$ to form active oxygen (e.g., O$_2^-$) due to the lower oxidation potential of e (−0.18 V vs NHE at pH = 1) than that of O$_2$ (e.g., O$_2$/O$_2^-$, −0.16 V vs NHE).[48−50] The holes oxidize donors: adsorbed H$_2$O or hydroxyl group on TiO$_2$ to produce hydroxyl radical (·OH), and adsorbed organic molecule (e.g., benzene) to form active organic molecules (e.g., benzene$^+$)[3,48−51] due to the higher oxidation potential of h (3.02 V vs NHE) than those of hydroxyl groups (e.g., OH·/OH$^-$, 1.89 V vs NHE)[50] and organic molecules (e.g., benzene, 2.995 V vs NHE).[52] Thus, the photocatalytic oxidation of organic molecule (e.g., benzene) proceeds.

Meanwhile, the light-driven thermocatalysis proceeds on the microsized mesoporous CeO$_2$. The widely accepted Mars−van Krevelen mechanism for the thermocatalytic oxidation on CeO$_2$ is as follows: organic molecule adsorbed on the surface of CeO$_2$ is oxidized by the lattice oxygen of CeO$_2$, and the reduced ceria is subsequently reoxidized by gas phase oxygen.[14,17,18,20]

The active benzene (e.g., benzene$^+$) produced by the photocatalysis on TiO$_2$ is more active than benzene according to molecular orbital theory as the electron number in the bonding molecular orbital of benzene$^+$ is less than that of benzene.[53] Thus, the reduction of CeO$_2$ by the active benzene is thermodynamically favorable. The active benzene undoubtedly migrates to CeO$_2$ through the interface of the TiO$_2$/CeO$_2$ nanocomposite, promoting the reduction of CeO$_2$ (Scheme 2) because the active benzene also existed on TiO$_2$ in the mixture of the nano TiO$_2$, and the microsized CeO$_2$ does not leads to an enhancement in the catalytic activity of CeO$_2$ (column a in Figure 5B and column e in Figure 6B). The active oxygen (e.g., O$_2^-$) and hydroxyl radical (·OH) produced by the photocatalysis on TiO$_2$ are more active than gas phase oxygen (O$_2$) in the convention thermocatalysis on CeO$_2$. Thus, the oxidation of the reduced ceria by the active oxygen (e.g., O$_2^-$) and hydroxyl radical (·OH) is thermodynamically favorable. The active species formed by the photocatalysis on TiO$_2$ migrate to CeO$_2$ via the interface of the TiO$_2$/CeO$_2$ nanocomposite, accelerating the oxidation of the reduced ceria formed by thermocatalyis (Scheme 2). Therefore, the synergetic effect between the photocatalysis on TiO$_2$ and the light-driven thermocatalysis on CeO$_2$ considerably increases the catalytic activity of the TiO$_2$/CeO$_2$ nanocomposites under the Xe lamp irradiation.

3.5. Origin of Synergetic Effect. It is widely accepted that the reducibility of CeO$_2$ plays a decisive role in its thermocatalytic activity, because the reduction of CeO$_2$ is much slower than the reoxidation of reduced ceria.[14,17,18,20] In order to put insight in the origin of the synergetic effect, the

effect of the irradiation on the reduction of CeO_2 is investigated by CO temperature-programmed reduction under the irradiation of the Xe lamp and in the dark (see Experimental Section). Under the dark condition without the irradiation of the Xe lamp, no peak is observed for pure TiO_2. A negative peak around 130 °C is observed for TiO_2/CeO_2-B due to the desorption of CO on CeO_2 (Figure 9A). Two broad TPR peaks
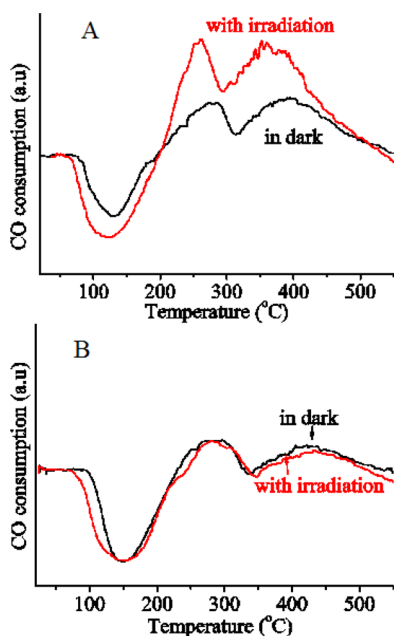
Figure 9. CO-TPR profile of TiO_2/CeO_2-B (A) and a mixture of TiO_2 and CeO_2 with the same Ti/Ce molar ratio as TiO_2/CeO_2-B (B) in the dark and with the irradiation of the Xe lamp.

around ~276, ~394 °C occur, which are attributed to the oxidation of CO by two types of surface lattice oxygen on CeO_2.[14,17] Interestingly, under the irradiation of the Xe lamp, the two broad TPR peaks shift to lower temperature of ~259, ~353 °C, respectively. This observation indicates that the irradiation of the Xe lamp reduces the oxidation temperature of CO by the lattice oxygen on CeO_2. Moreover, the intensity of the two TPR peaks is considerably enhanced. We quantitatively measure the amounts of CO consumed for TiO_2/CeO_2-B by calculating the area of their TPR profiles calibrated by the reduction of a known amount of CuO by CO. The total amounts of CO consumed for TiO_2/CeO_2-B in the dark is 580.1 μmol g^{-1}. Under the irradiation of the Xe lamp, the total amounts of CO consumed increases to 1033.1 μmol g^{-1}. In striking contrast, for a mixture of the nano TiO_2 and the microsized mesoporous CeO_2 with the same Ti/Ce molar ratio as TiO_2/CeO_2-B, the irradiation of the Xe lamp does not lead to an obvious evolution of its CO-TPR profile as compared to that in the dark (Figure 9B). This result reveals that the irradiation of the Xe lamp significantly accelerates the reduction of CeO_2 by CO for the TiO_2/CeO_2 nanocomposite, and the promotion of CeO_2 reduction by CO with the irradiation occurs at the interface of the TiO_2/CeO_2 nanocomposite. Munoz-Batista repoted that the reaction rate behavior in the TiO_2/CeO_2 composite system was dominated by the availability of holes at the surface of the material, and the photodegradation was a hole-triggered reaction.[27] For CO-TPR in dark, there is only the reduction of CeO_2 by CO. For CO-TPR under the irradiation of the Xe lamp, the photogenerated

hole (h) on TiO_2 reacts with CO to form active CO (e.g., CO$^+$) due to the higher oxidation potential of h than that of CO (0.64 V vs RHE on Pt electrode).[54] The active CO (e.g., CO$^+$) is more active than CO according to molecular orbital theory as the electron number in the bonding molecular orbital of CO$^+$ is less than that of CO.[53] Thus, the reduction of CeO_2 by the active CO (e.g., CO$^+$) is thermodynamically favorable. The active CO (e.g., CO$^+$) produced by photocatalysis on TiO_2 undoubtedly migrates to CeO_2 through the interface of the TiO_2/CeO_2 nanocomposites, promoting the reduction of CeO_2 (Figure 9A) because the active CO, also existing on TiO_2 in the mixture of the nano TiO_2 and the microsized CeO_2, does not leads to the promotion of CeO_2 reduction (Figure 9B). This accounts for the shift of the CO-TPR peaks to lower temperature as well as the enhancement of CO consumption with the irradiation of the Xe lamp for the TiO_2/CeO_2 nanocomposite (Figure 9A). It should be noted that, in principle, photogenerated electrons and holes could be produced on the conduction band and valence band of CeO_2 upon UV or visible irradiation, respectively.[27,31] However, the photogenerated holes on CeO_2 do not promote the reduction of CeO_2 (Figure 9B). The considerable promotion of CeO_2 reduction by the photocatalysis on TiO_2 rather than by the photocatalysis on CeO_2 improves the solar-light-driven thermocatalytic activity of CeO_2 for the TiO_2/CeO_2 nanocomposite, as illustrated in Scheme 2.

4. CONCLUSION

In summary, TiO_2/CeO_2 nanocomposites exhibit enhanced catalytic activity for benzene oxidation under the irradiation of the Xe lamp compared to pure CeO_2 and TiO_2. A solar-light-driven thermocatalysis on CeO_2 is found for the TiO_2/CeO_2 nanocomposites. There is a synergetic effect between the photocatalysis on TiO_2 and the thermocatalysis on CeO_2 for the TiO_2/CeO_2 nanocomposites, which significantly increases their catalytic activity. The synergetic effect, which occurs at the interface of the TiO_2/CeO_2 nanocomposites, is due to the considerable promotion of the CeO_2 reduction by the photocatalysis on TiO_2. The novel strategy using the synergetic effect between the photocatalysis on TiO_2 and the solar-light-driven thermocatalysis on CeO_2 is applicable for designing other nanocomposite catalysts for the environmental purification using renewable solar energy.

■ ASSOCIATED CONTENT

Ⓢ Supporting Information
The following file is available free of charge on the ACS Publications website at DOI: 10.1021/acscatal.5b00292.

    SEM and N_2 adsorption−desorption of the catalysts (PDF)

■ AUTHOR INFORMATION

Corresponding Author
*E-mail: liyuanzhi66@hotmail.com.

Notes
The authors declare no competing financial interest.

■ ACKNOWLEDGMENTS

■ REFERENCES

(1) Huang, Q. W.; Tian, S. Q.; Zeng, D. W.; Wang, X. X.; Song, W. L.; Li, Y. Y.; Xiao, W.; Xie, C. S. *ACS Catal.* **2013**, *3*, 1477−1485.

(2) Hou, J. T.; Li, Y. Z.; Liu, L. L.; Ren, L.; Zhao, X. J. *J. Mater. Chem. A* **2013**, *1*, 6736−6741.

(3) Chen, X. B.; Mao, S. S. *Chem. Rev.* **2007**, *107*, 2891−2959.

(4) Kong, M.; Li, Y. Z.; Chen, X.; Tian, T. T.; Fang, P. F.; Zheng, F.; Zhao, X. J. *J. Am. Chem. Soc.* **2011**, *133*, 16414−1617.

(5) Tang, J. W.; Durrant, J. R.; Klug, D. R. *J. Am. Chem. Soc.* **2008**, *130*, 13885−13891.

(6) Asahi, R.; Morikawa, T.; Ohwaki, T.; Aoki, K.; Taga, Y. *Science* **2001**, *293*, 269−271.

(7) Shi, N.; Li, X. H.; Fan, T. X.; Zhou, H.; Ding, J. A.; Zhang, D.; Zhu, H. X. *Energy Environ. Sci.* **2011**, *4*, 172−180.

(8) Li, Y. F.; Xu, D. H.; Oh, J. I.; Shen, W. Z.; Li, X.; Yu, Y. *ACS Catal.* **2012**, *2*, 391−398.

(9) Mendez-Roman, R.; Cardona-Martinez, N. *Catal. Today* **1998**, *40*, 353−365.

(10) Wu, W.; Liao, L.; Lien, C.; Lin, J. *Phys. Chem. Chem. Phys.* **2001**, *3*, 4456−4461.

(11) Li, Y. Z.; Huang, J. C.; Peng, T.; Xu, J.; Zhao, X. J. *ChemCatChem* **2010**, *2*, 1082−1087.

(12) Liotta, L. F. *Appl. Catal., B* **2010**, *100*, 403−412.

(13) Zhang, D. S.; Du, X. J.; Shi, L. Y.; Gao, R. H. *Dalton Trans.* **2012**, *41*, 14455−14475.

(14) Wu, Z. L.; Li, M. J.; Overbury, S. H. *J. Catal.* **2012**, *285*, 61−73.

(15) Mai, H. X.; Sun, L. D.; Zhang, Y. W.; Si, R.; Feng, W.; Zhang, H. P.; Liu, H. C.; Yan, C. H. *J. Phys. Chem. B* **2005**, *109*, 24380−24385.

(16) Zhang, J.; Kumagai, H.; Yamamura, K.; Ohara, S.; Takami, S.; Morikawa, A.; Shinjoh, H.; Kaneko, K.; Adschiri, T.; Suda, A. *Nano Lett.* **2011**, *11*, 361−364.

(17) Liu, X. W.; Zhou, K. B.; Wang, L.; Wang, B. Y.; Li, Y. D. *J. Am. Chem. Soc.* **2009**, *131*, 3140−3141.

(18) Lawrence, N. J.; Brewer, J. R.; Wang, L.; Wu, T. S.; Wells-Kingsbury, J.; Ihrig, M. M.; Wang, G. H.; Soo, Y. L.; Mei, W. N.; Cheung, C. L. *Nano Lett.* **2011**, *11*, 2666−2671.

(19) Hua, G. M.; Zhang, L. D.; Fei, G. T.; Fang, M. *J. Mater. Chem.* **2012**, *22*, 6851−6855.

(20) Shi, W. Q.; Li, Y. Z.; Hou, J. T.; Lv, H. Q.; Zhao, X. J.; Fang, P. F.; Zheng, F.; Wang, S. J. *J. Mater. Chem. A* **2013**, *1*, 728−734.

(21) Ji, P. F.; Zhang, J. L.; Chen, F.; Anpo, M. *J. Phys. Chem. C* **2008**, *112*, 17809−17813.

(22) Valente, J. S.; Tzompantzi, F.; Prince, J. *Appl. Catal., B* **2011**, *102*, 276−285.

(23) Chaudhary, Y. S.; Panigrahi, S.; Nayak, S.; Satpati, B.; Bhattacharjee, S.; Kulkarni, N. *J. Mater. Chem.* **2010**, *20*, 2381−2385.

(24) Hernandez-Alonso, M. D.; Hungría, A. B.; Martínez-Arias, A.; Fernandez-García, M.; Coronado1, J. M.; Conesa, J. C.; Soria, J. *Appl. Catal., B* **2004**, *50*, 167−175.

(25) Yue, L.; Zhang, X. M. *J. Alloys Compd.* **2009**, *475*, 702−705.

(26) Channei, D.; Inceesungvorn, B.; Wetchakun, N.; Ukritnukun, S.; Nattestad, A.; Chen, J.; Phanichphant, S. *Sci. Rep.* **2014**, *4*, 5757.

(27) Munnoz-Batista, M. J.; Gomez-Cerezo, M. N.; Kubacka, A.; Tudela, D.; Fernandez-Garcia, M. *ACS Catal.* **2014**, *4*, 63−72.

(28) Parasupree, S.; Suzuki, Y.; Prisa-Art, S.; Yoshikawa, S. *J. Solid State Chem.* **2005**, *178*, 128−134.

(29) Ghasemi, S.; Setayesh, S. R.; Habibi-Yangjeh, A.; Hormozi-Nezhad, M. R.; Gholami, M. R. *J. Hazard. Mater.* **2012**, *199- 200*, 170−178.

(30) Li, G.; Zhang, D.; Yu, Y. C. *Phys. Chem. Chem. Phys.* **2009**, *11*, 3775−3782.

(31) Tian, J.; Sang, Y. H.; Zhao, Z. H.; Zhou, W. J.; Wang, D. Z.; Kang, X. L.; Liu, H.; Wang, J. Y.; Chen, S. W.; Cai, H. Q.; Huang, H. *Small* **2013**, *9*, 3864−3872.

(32) Cao, T. P.; Li, Y. J.; Wang, C. H.; Wei, L. M.; Shao, C. L.; Liu, Y. C. *Mater. Res. Bull.* **2010**, *45*, 1406−1412.

(33) Wang, Y. G.; Li, B.; Zhang, C. L.; Cui, L. F.; Kang, S. F.; Li, X.; Zhou, L. H. *Appl. Catal., B* **2013**, *130- 131*, 277−284.

(34) Yang, H. M.; Zhang, K.; Shi, R. R. *J. Am. Ceram. Soc.* **2007**, *90*, 1370−1374.

(35) Karunakaran, C.; Gomathisankar, P. *ACS Sustainable Chem. Eng.* **2013**, *1*, 1555−1563.

(36) Alessandri, I.; Zucca, M.; Ferroni, M.; Bontempi, E.; Depero, L. E. *Small* **2009**, *5*, 336−340.

(37) Lin, H.; Wang, M.; Wang, Y.; Liang, Y.; Cao, W.; Su, Y. *J. Photochem. Photobiol., A* **2011**, *223*, 157−162.

(38) Wang, Y.; Li, B.; Zhang, C.; Cui, L.; Kang, S.; Li, X.; Zhou, L. *Appl. Catal., B* **2013**, *130−131*, 277−284.

(39) Munnoz-Batista, M. J.; Kubacka, A.; Gomez-Cerezo, M. N.; Tudela, D.; Fernaandez-Garcia, M. *Appl. Catal., B* **2013**, *140−141*, 626−635.

(40) Li, Y. Z.; Sun, Q.; Kong, M.; Shi, W. Q.; Huang, J. C.; Tang, J. W.; Zhao, X. J. *J. Phys. Chem. C* **2011**, *115*, 14050−14057.

(41) Jiang, D.; Wang, W. Z.; Gao, E.; Zhang, L.; Sun, S. *J. Phys. Chem. C* **2013**, *117*, 24242−24249.

(42) Jiang, D.; Wang, W. Z.; Zhang, L.; Qiu, R. H.; Sun, S. M.; Zheng, Y. L. *Appl. Catal., B* **2015**, *165*, 399−407.

(43) Liyanage, A. D.; Perera, S. D.; Tan, K.; Chabal, Y.; Balkus, K. J., Jr. *ACS Catal.* **2014**, *4*, 577−584.

(44) (a) Hou, J. T.; Li, Y. Z.; Mao, M. Y.; Yue, Y. Z.; Greaves, G. N.; Zhao, X. J. *Nanoscale* **2015**, *7*, 2633−2640. (b) Ma, Y.; Li, Y. Z.; Mao, M. Y.; Hou, J. T.; Zeng, M.; Zhao, X. J. *J. Mater. Chem. A* **2015**, *3*, 5509−5516. (c) Mao, M. Y.; Li, Y. Z.; Hou, J. T.; Zeng, M.; Zhao, X. J. *Appl. Catal., B* **2015**, *174-175*, 496−503.

(45) Zhang, Y. H.; Ebbinghaus, S. G.; Weidenkaff, A.; Kurz, T.; von Nidda, H. A. K.; Klar, P. J.; Gungerich, M.; Reller, A. *Chem. Mater.* **2003**, *15*, 4028−4033.

(46) Patsalas, P.; Logothetidis, S.; Sygellou, L.; Kennou, S. *Phys. Rev. B: Condens. Matter Mater. Phys.* **2003**, *68*, 035104.

(47) Salvi, A. M.; Decker, F.; Varsano, F.; Speranza, G. *Surf. Interface Anal.* **2001**, *31*, 255−264.

(48) Linsebigler, A. L.; Lu, G. Q.; Yates, J. T., Jr. *Chem. Rev.* **1995**, *95*, 735−758.

(49) Sawyer, D. T.; Valentine, J. S. *Acc. Chem. Res.* **1981**, *14*, 393−400.

(50) Tachikawa, T.; Fujitsuka, M.; Majima, T. *J. Phys. Chem. C* **2007**, *111*, 5259−5275.

(51) d'Hennezel, O.; Pichat, P.; Ollis, D. F. *J. Photochem. Photobiol., A* **1998**, *118*, 197−204.

(52) Luo, L.; Li, Y. Z.; Hou, J. T.; Yang, Y. *Appl. Surf. Sci.* **2014**, *319*, 332−338.

(53) Zhou, G. D.; Duan, Y. L. *The Basis of Structural Chemistry*; Peking University Press: Peking, China, 2008; pp 1−363.

(54) Ianniello, R.; Schmidt, V. M.; Stimming, U.; Super, J.; Wallau, A. *Electrochim. Acta* **1994**, *39*, 1863−1869.